

# Spinning nano-carbon grains: a viable origin for the Anomalous Microwave Emission

N. Ysard<sup>1</sup>, M.-A. Miville-Deschénes<sup>2</sup>, L. Verstraete<sup>1</sup>, and A.P. Jones<sup>1</sup>

<sup>1</sup> Université Paris-Saclay, CNRS, Institut d'astrophysique spatiale, 91405, Orsay, France

<sup>2</sup> AIM, CEA, CNRS, Université Paris-Saclay, Université Paris Diderot, Sorbonne Paris Cité, 91191 Gif-sur-Yvette, France  
e-mail: nathalie.ysard@universite-paris-saclay.fr

Preprint online version: May 4, 2022

## ABSTRACT

**Context.** Excess microwave emission commonly known as ‘anomalous microwave emission’ (AME) is now routinely detected in the Milky Way. Although its link with the rotation of interstellar (carbonaceous) nano-grains seems to be relatively well established at cloud scales, large-scale observations show a lack of correlation between the different tracers of nano-carbons and AME, which has led the community to question the viability of this link.

**Aims.** Using ancillary data and spinning dust models for nano-carbons and nano-silicates, we explore the extent to which the out of Galactic Plane AME could come from one carrier or the other.

**Methods.** Contrary to previous large-scale studies, our method is not built on comparing the correlations of the different dust tracers with each other, but rather on comparing the poor correlations predicted by the models with the correlations actually observed. This is based on as realistic as possible estimates of the gas ionisation state and grain charge as a function of the local radiation field and gas density.

**Results.** First, nano-carbon dust can explain all the observations for medium properties in agreement with the latest findings about the separation of cold and warm neutral medium in the diffuse ISM. The dispersion in the observations can be accounted for with little variations in the dust size distribution, abundance or electric dipole moment. Second, whatever the properties and the abundance of the nano-silicate dust considered, spinning nano-silicates are excluded as being the sole source of the AME. Third, the best agreement with the observations is obtained if the emission of spinning nano-carbons alone is taken into account. However, a marginal participation of nano-silicates to the AME production cannot be excluded as long as their abundance does not exceed  $Y_{\text{Si}} \sim 1\%$ .

**Key words.** ISM: general - ISM: dust, emission, extinction

## 1. Introduction

First detected in the 1990s as a dust-correlated excess component above the free-free and synchrotron emissions (e.g. Kogut et al. 1996; Leitch et al. 1997), the ‘Anomalous Microwave Emission’ (AME) has since been observed to be bright in the Milky Way and other galaxies (see the review by Dickinson et al. 2018), with coherent AME structures from scales of degrees down to arcseconds. The prevalent explanation is that AME’s carriers are spinning carbonaceous nano-grains emitting through spontaneous emission of purely rotational photons (e.g. Draine & Lazarian 1998a; Ali-Haïmoud et al. 2009; Ysard & Verstraete 2010; Ysard et al. 2010; Silsbee et al. 2011). Yet other carriers of nanometric size such as spinning nano-silicates may also contribute to AME (Hoang et al. 2016; Hensley & Draine 2017). Other AME origins were also suggested, such as spinning grain magnetic dipole emission (Draine & Hensley 2013; Hoang & Lazarian 2016), thermal emission from magnetic dust (Draine & Lazarian 1999) and variations in the submillimetre opacity of amorphous solids at low temperature (Jones 2009; Nashimoto et al. 2020), all of them having some trouble reconciling with the low polarisation degree of the 30 GHz AME, which is less than 1% in the diffuse interstellar medium (see Table 4 in Dickinson et al. 2018, and references therein).

AME is a bright component that accounts for about half of the observed intensity at 30 GHz in the Galactic Plane (Planck Collaboration et al. 2014b, 2016c,b). It is brightest in interstel-

lar regions hosting photon-dominated regions (PDRs, Casassus et al. 2008, 2021; Cepeda-Arroita et al. 2021; Tibbs et al. 2010, among others). These highly irradiated transition regions between HII regions and molecular clouds are known to be sites of strong and rapid evolution of the sub-nanometre hydrocarbon grain populations. Many studies have shown that the abundance of the carbonaceous nano-grains decreases while their minimum size increases when moving from the outer PDRs to the inner molecular clouds. This holds true regardless of the assumed type of carbonaceous nano-grains, *i.e.*, PAHs (e.g. Berné et al. 2007; Compiègne et al. 2008; Arab et al. 2012; Pilleri et al. 2012, 2015) or amorphous hydrocarbons a-C(H) (Schirmer et al. 2020), and is taken to be the result of photoprocessing in all cases (see for instance Murga et al. 2016, 2019). Casassus et al. (2021) showed that this scenario is consistent with AME ATCA observations of the  $\rho$  Oph W PDR at an angular resolution of 30''. They found that the peak frequency of the AME increases from the inner to the outer PDR and that the correlation with mid-IR emission in the Spitzer IRAC 8  $\mu\text{m}$  filter is tight in the inner PDR but less so towards the exciting star. Fitting these data with spinning PAHs was possible by adopting an increase in the minimum size deeper into the PDR, in agreement with previous PDR studies based on near- to far-IR observations. As stated by Casassus et al. (2021), at small scales the AME appears to correlate tightly with the carbonaceous nano-grain mid-IR emission. This was also shown to be the case for other PDRs (e.g. Casassus et al. 2008; Tibbs et al. 2010, 2011; AMI Consortium: Scaife et al. 2010; Bell et al.

2019; Cepeda-Arroita et al. 2021) and the dark clouds LDN1622 and LDN1780 (Harper et al. 2015; Vidal et al. 2020, respectively). Vidal et al. (2020) found that the observed variations in the 30 GHz emissivity observed in LDN1780 are consistent with spinning PAHs, with size distribution variations from the outer layers to the dense core of the molecular cloud, in agreement with the 3D radiative transfer modelling of IR data performed by Ridderstad et al. (2006).

These small-scale studies clearly illustrate that, despite the good agreement between the spinning carbonaceous nano-grain emission model and the observed AME, the correlation between the mid-IR emission and the AME can actually be rather poor. This is especially true in the high radiation field or high density bright regions dominated lines of sight, for example along the Galactic Plane. The starting point of our study is to address the challenge to the validity of the rotating carbonaceous nano-grain origin of the AME by Hensley et al. (2016). Performing a full-sky analysis at a  $1^\circ$  angular resolution, their conclusions were based on the poor correlation of the 30 GHz AME with the observed mid-IR emission and on the way the AME correlates with the dust far-IR to submm radiance. They concluded that other carriers, such as nano-silicates, or that other emission mechanisms, had to be considered. Using the same AME data as Hensley et al. (2016), we perform a full-sky analysis with the aim of reconciling the small and large scale observations. However, our method does not compare the correlations between the different dust tracers, but, in agreement with small scale studies, compares the poor correlations predicted by the models with the correlations actually observed. In order to be comprehensive we consider both spinning nano-silicate and nano-carbon dust emission.

The paper is organised as follows. Section 2 describes the data sets and Sect. 3 the dust properties and spinning dust model used. We then discuss the latest observational findings on the density of the neutral gas and its distribution in the diffuse interstellar medium in Sect. 4. Our results are presented in Sect. 3.3 and we finally give our conclusions in Sect. 6.

## 2. Observational data

To carry out our analysis, in addition to maps of the AME, we use data characteristic of the thermal emission of grains, both big and small, as well as of the radiation field and the column density.

### 2.1. Planck LFI and HFI foreground products

The Planck observatory<sup>1</sup> carried out a full-sky survey in nine frequency channels between 30 and 857 GHz, i.e.  $\sim 1$  cm and  $350\ \mu\text{m}$ , which was subsequently used to estimate the diffuse Galactic emission components: AME, dust thermal emission, free-free and synchrotron emissions.

For the AME, we use the decomposition made by Planck Collaboration et al. (2016b) which combined the Planck temperature maps in all the Low Frequency Instrument (LFI: 30, 44 and 70 GHz) and High Frequency Instrument (HFI: 100, 143,

<sup>1</sup> Planck (<http://www.esa.int/Planck>) is a project of the European Space Agency (ESA) with instruments provided by two scientific consortia funded by ESA member states and led by Principal Investigators from France and Italy, telescope reflectors provided through a collaboration between ESA and a scientific consortium led and funded by Denmark, and additional contributions from NASA (USA).

353 and 857 GHz) channels, the 9-yr sky maps of the Wilkinson Microwave Anisotropy Probe (WMAP: five channels from 23 to 94 GHz, Bennett et al. 2013), and the Haslam et al. (1982) 408 MHz map. This allowed Planck Collaboration et al. (2016b) to deliver a parametric model of AME at an angular resolution of  $1^\circ$ . The model parameters are available as a Healpix map (Górski et al. 2005) with  $n_{\text{side}} = 256$  that can be downloaded from the Planck Legacy Archive<sup>2</sup> (PLA). With those, we compute AME maps at 20, 30 and 40 GHz.

Planck Collaboration et al. (2014a) combined the Planck HFI maps with the IRIS 100  $\mu\text{m}$  map (Miville-Deschénes & Lagache 2005). Performing a pixel-by-pixel modified blackbody  $\chi^2$  fit, Planck Collaboration et al. (2014a) derived the dust far-IR radiance,  $R = \int_v I_v dv$ , and optical depth at 353 GHz,  $\tau_{353\text{GHz}}$ . These product maps can be downloaded from the PLA as Healpix maps with a  $1^\circ$  angular resolution and  $n_{\text{side}} = 256$ . The radiance is useful as a good proxy for the radiation field and the optical depth gives an estimate of the emissivity of big grains, in principle independent of temperature. Both of these assertions are, however, questionable in the dense molecular regions were large variations in the temperature along the line of sight and variations in the dust grain optical properties are expected (e.g. Planck Collaboration et al. 2014a).

### 2.2. Thermal dust emission

To characterise the big grain thermal emission, we use the 100  $\mu\text{m}$  map described in Planck Collaboration et al. (2014a). It is a combination of the map of Schlegel et al. (1998) at scales larger than  $30'$  and the IRIS map of Miville-Deschénes & Lagache (2005) at smaller scales. This combination provides the better large scale structure of the Schlegel et al. (1998) map, less contaminated by zodiacal light residuals, with the higher resolution and better calibration of the IRIS map (see Sect. 2.2 in Planck Collaboration et al. 2014a, for details). The IRIS maps are derived from the IRAS data and have an angular resolution of  $5'$ , central wavelengths of 12, 25, 60 and 100  $\mu\text{m}$  with bandwidth of  $\sim 7.0, 11.15, 32.5$  and  $31.5\ \mu\text{m}$  (Wheelock et al. 1994; Miville-Deschénes & Lagache 2005).

In addition, the nano-grain thermal emission is characterised using the 12  $\mu\text{m}$  IRIS map (Miville-Deschénes & Lagache 2005) from which zodiacal residuals were filtered out using a matched filter technique tailored to extract diffuse emission correlated to the ecliptic reference frame. The technique used is described in Appendix A. The 12 and 100  $\mu\text{m}$  IRIS maps are smoothed to  $\text{FWHM} = 1^\circ$  and projected on a  $n_{\text{side}} = 256$  Healpix grid.

### 2.3. Column density map

As stated in Sect. 1, our postulate is that AME is produced by the rotation of (sub)nanometric sized grains which radiate most of their energy in the near- to mid-IR. It has been known for decades that the dust SED in this spectral range varies a lot depending on the observed ISM regions (e.g. Laureijs et al. 1991; Abergel et al. 1996; Berné et al. 2007). These variations are commonly interpreted in terms of variations in the size distribution and abundance of nano-grains (see Ridderstad et al. 2006; Vidal et al. 2020; Casassus et al. 2021, for AME related examples). In particular, there is a deficit in the mid-IR relative to the far-IR emission when comparing atomic diffuse lines of sight to those containing molecular clouds which can be explained by the disappearance of the small nano-grains in tandem with

<sup>2</sup> <http://pla.esac.esa.int/pla/>.

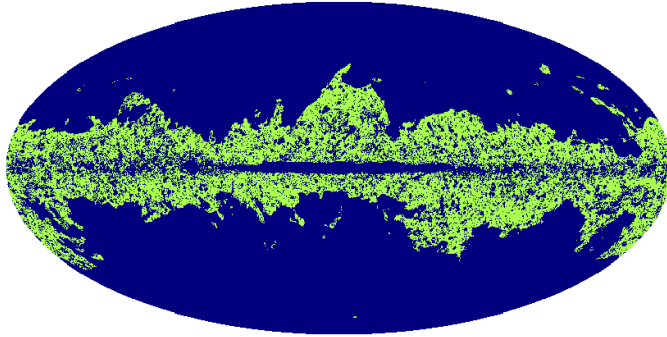


**Fig. 1.** Mask used to make the analysis, green pixels are those used.

the growth of the larger grains by grain-grain coagulation (e.g. Bernard et al. 1999; Stepnik et al. 2003; Flagey et al. 2009; Ysard et al. 2013). Such a disappearance is in agreement with the variations observed in the 2175 Å bump towards molecular clouds (e.g. Mathis & Whiffen 1989; Kim et al. 1994; Campeggio et al. 2007) while the growth of the larger grains can explain the observed increase in selective extinction  $R_V$  (e.g. Ormel et al. 2009; Köhler et al. 2015).

Furthermore, all models, regardless of their specifics in terms of composition and initial grain size distribution, indicate that the disappearance of the nano-grains occurs – and the growth of larger grains starts occurring – at still relatively low densities of the order of (a few)  $10^3$  H/cm<sup>3</sup>. This has been shown from observations of (i) the thermal emission of grains from the mid- to far-IR (e.g. Ridderstad et al. 2006; Ysard et al. 2013; Saajasto et al. 2021) ; (ii) the near- to mid-IR scattering known as cloudshine and coreshine (e.g. Lefèvre et al. 2014; Ysard et al. 2016; Juvela et al. 2020) ; and (iii) the polarisation (e.g. Fanciullo et al. 2017; Vaillancourt et al. 2020). Depending on the dust model details and the gas local properties, the accretion of the (sub)nanometric grains on larger grains is not expected to take more than a hundred to a few thousand years in the outskirts of molecular clouds (e.g. Stepnik et al. 2003; Köhler et al. 2012; Ysard et al. 2013; Jones et al. 2014). Therefore, if we start from the assumption that nano-grains are responsible for the AME, then the microwave flux must come primarily from the atomic diffuse ISM and the HI column density is the one that should be used when modelling both the AME and the 12 μm emission.

Consequently, the HI column density map used in this study is the one of the HI4PI survey (HI4PI Collaboration et al. 2016). It was constructed by adding all velocity channels between -90 and +90 km s<sup>-1</sup> to avoid High-Velocity Clouds emission. The native angular resolution of this map is FWHM = 16.2'. It was then convolved with the required complementary Gaussian beam to bring the map to FWHM = 1° before reprojecting to a  $n_{\text{side}} = 256$  Healpix grid.

#### 2.4. Masks

In the following, we exclude a number of pixels from our analysis. First, as we focus on the neutral diffuse medium, we exclude the Galactic Plane which contains many molecular regions as well as very bright HII complexes (e.g. Cygnus X) that are too complicated to be modelled globally. To do so, we use the mask

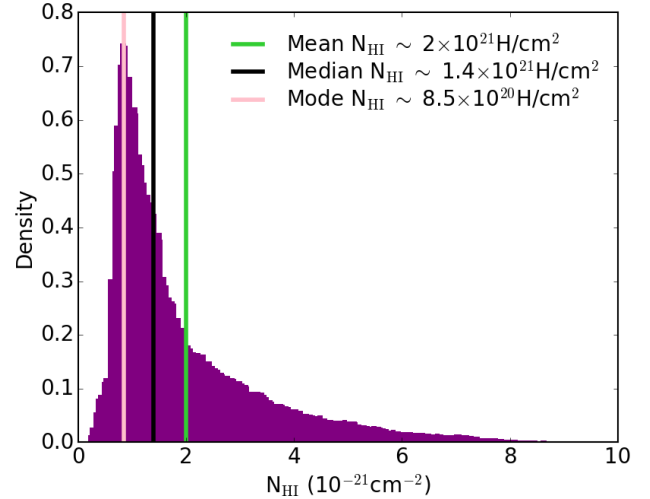


**Fig. 2.** Histogram of the column density of the pixels selected for the analysis.

defined by Planck Collaboration et al. (2016a), based on the intensity at 353 GHz, excluding 1% of the sky. We also exclude the point sources detected in the six Planck HFI frequency channels at 100, 143, 217, 353, 545 and 857 GHz, and in the Planck LFI 30 GHz channel (Planck Collaboration et al. 2016a). This results in excluding  $\sim 23\%$  of the sky for Healpix maps with  $n_{\text{side}} = 256$ . A third mask is applied to the data to exclude pixels for which the  $S/N < 3$  in the 30 GHz AME map. This leads to the rejection of high Galactic latitude pixels for which the AME intensity is very low and covering less than 1% of the sky. According to Planck Collaboration et al. (2016c), the component separation solution in these pixels is dominated by instrumental noise. Finally, we remove the sky area where the  $S/N < 3$  in the 12 μm IRIS map. The uncertainty in these mainly high latitude areas is dominated by the uncertainty in the subtraction of the zodiacal emission. This amounts to eliminating  $\sim 63\%$  of the sky. The resulting mask is displayed in Fig. 1. It mainly excludes the Galactic Plane and the highest latitude regions, i.e. about 76% of the sky.

This leads to data with column densities ranging from  $\sim 10^{20}$  to  $1.4 \times 10^{22}$  H/cm<sup>2</sup> (Fig. 2). The mean, median and mode of the column density distribution are  $\sim 2 \times 10^{21}$ ,  $1.4 \times 10^{21}$  and  $8.5 \times 10^{20}$  H/cm<sup>2</sup>, respectively. The standard deviation is  $\sim 1.5 \times 10^{21}$  H/cm<sup>2</sup>.

### 3. Models: spinning and thermal dust emission

All estimates presented in the following are obtained with the numerical code DustEM<sup>3</sup> (Compiègne et al. 2011). DustEM is a versatile numerical tool mainly used to calculate the extinction and thermal emission (polarised or not) of any grain model. A calculation of the spinning dust emission is also implemented. The specificity of this implementation is that it allows the user to process in a consistent way all the parameters involved in the calculation of the excitation and damping of the grain rotation according to their size and composition.

The rate of grain rotation depends on their emission of rovibrational and rotational photons, and how they interact with the gas. To quantify these interactions, it is necessary to know the

<sup>3</sup> Available here: <https://www.ias.u-psud.fr/DUSTEM/>.

charge distribution of the grains and the main parameters describing the state of the gas. These parameters are its temperature  $T_{\text{gas}}$ , the electron abundance  $x_e = n_e/n_{\text{H}}$ , the molecular fraction  $y = n(\text{H}_2)/n_{\text{H}}$  and the ionisation fraction of the major species:  $x_{\text{H}} = n(\text{HII})/n_{\text{H}}$ ,  $x_{\text{C}} = n(\text{CII})/n_{\text{H}}$  where  $n_{\text{H}} = n(\text{HI}) + n(\text{HII}) + 2n(\text{H}_2)$ . The equilibrium charge distribution  $f(Z)$  of grains per size and type is computed using the Kimura (2016) model for the photoemission yield and the Weingartner & Draine (2001) formalism for the remaining processes<sup>4</sup>. In turn, the parameters describing the gas state are computed using the formalism described in Ysard et al. (2011).

### 3.1. Dust properties

The dust properties used are those of The Heterogeneous dust Evolution Model for Interstellar Solids (THEMIS<sup>5</sup>, Jones et al. 2017). It assumes that dust in the diffuse ISM consists of small nano-grains of aromatic-rich carbon (radius  $0.4 \leq a \leq 20$  nm) and larger core-mantle grains, for which the cores are composed either of amorphous aliphatic-rich carbon or of a mixture of amorphous silicates with the normative chemical compositions of olivine and pyroxene (with half of the total mass of silicate grains in each type). For all types of grains, the mantles are made of aromatic-rich carbons with a thickness of 20 nm for the carbon cores and 5 nm for the silicate cores. Moreover, iron and sulphur are incorporated into the silicate cores in the form of metallic nano-inclusions of Fe and FeS. They represent 10% of the total core volume, of which 30% is FeS and 70% is pure Fe. This model allows to reproduce the emission and extinction curves representative of the diffuse medium at high Galactic latitude from the optical to the submillimetre (c.f. Jones et al. 2013; Ysard et al. 2015).

To model spinning nano-carbon dust emission, we use the by-default size distribution of THEMIS which is a power-law  $\propto a^{-5}$  with an exponential cut-off and a minimum size of 0.4 nm. We assume their permanent electric dipole moment to be  $\mu \sim m \sqrt{N_{\text{at}}}$  where  $N_{\text{at}}$  is the number of atoms in the grain and  $m = 0.38$  D (see references in Draine & Lazarian 1998b). The THEMIS nano-carbon grains have (Jones 2012a,b,c):

$$N_{\text{at}} = 2500 \left( \frac{a}{1 \text{ nm}} \right) \left( \frac{\rho}{12 - 11X_{\text{H}}} \right), \quad (1)$$

where  $X_{\text{H}}$  is the grain hydrogen fraction and  $\rho$  its density, which are equal to 0.023 and 1.6 g/cm<sup>3</sup> for the nano-carbons of interest for rotational emission.

THEMIS does not include nano-silicates. Indeed, to date, the observations have not provided any evidence of their presence in the diffuse medium. However, this lack of detection does not rule them out as a minority constituent and other dust models include nano-silicates and have put tentative upper limits on their abundance (e.g. Désert et al. 1986; Li & Draine 2001). To model spinning nano-silicate dust emission, in addition to the THEMIS dust components, we follow the studies of Hoang et al. (2016) and Hensley & Draine (2017) to define a size distribution for nano-silicates and set their electric dipole moment and abundance. According to these two studies, to be able to explain AME by the rotation of nano-silicates without contradicting other observations, they cannot contain more than 14% of the available silicon and their dipole moment per atom must be  $0.2 \leq m \leq 1$  D. To estimate the nano-silicate dipole moments, we assume that

<sup>4</sup> Details about the model can be found here: <https://www.ias.u-psud.fr/DUSTEM/userguide.html>.

<sup>5</sup> Available here: <https://www.ias.u-psud.fr/themis/>.

they are a 50%-50% mixture of grains having the normative compositions of forsterite and enstatite to calculate the number of atoms as a function of their size. For the size distribution, both studies assumed log-normal distributions centred on a sub-nanometric size  $a_0$  and of variable width  $\sigma$ . Contrary to Hoang et al. (2016), Hensley & Draine (2017) took into account the sublimation rates calculated by Guhathakurta & Draine (1989) to set a minimum nano-silicate grain size, who found that when illuminated by the average interstellar radiation field the critical survival size is of 37 atoms, i.e. about 0.45 nm. For the models presented in the following, assuming that  $Y_{\text{Si}} = 10\%$  of the total silicon included in dust is locked in nano-silicates, upper limit derived by Li & Draine (2001), and that  $a_0 = a_{\text{min}} = 0.45$  nm as in Hensley & Draine (2017), we define four cases:

- case 1:  $m = 0.3$  D and  $\sigma = 0.3$  ;
- case 2:  $m = 0.3$  D and  $\sigma = 0.1$  ;
- case 3:  $m = 1$  D and  $\sigma = 0.3$  ;
- case 4:  $m = 1$  D and  $\sigma = 0.1$ .

This roughly covers the parameter space defined as acceptable by Hoang et al. (2016) and Hensley & Draine (2017).

### 3.2. Local medium properties

To compare with observations, model grids are generated for nano-carbons and nano-silicates. Once the dust properties are settled, DustEM only requires three inputs: the radiation field, the gas density and the gas temperature.

We assume that the interstellar radiation field illuminating the grains has the same spectral distribution as the field of Mathis et al. (1983). Its intensity is then scaled by the  $G_0$  factor with  $0.1 \leq G_0 \leq 20$ ,  $G_0 = 1$  corresponding to the Mathis et al. (1983) standard field intensity in the solar neighbourhood. For the gas, we start from a very diffuse medium with  $n_{\text{H}} = 0.05$  H/cm<sup>3</sup> to go to densities representative of translucent clouds with  $n_{\text{H}} = 1\,000$  H/cm<sup>3</sup>. This wide range of parameters should a priori make it possible to account for the physical conditions of most of the out of Galactic plane lines of sight considered in this study. The corresponding gas temperatures are computed with CLOUDY (Ferland et al. 1998). The other gas parameters are directly calculated by DustEM (see Ysard et al. 2011, for details).

### 3.3. Resulting spectral energy distributions (SEDs)

We show two sets of modelling results in Fig. 3. Firstly, the left panel shows the emission spectra of media with  $G_0 = 1$  and local gas densities of  $n_{\text{H}} = 0.1$  and 30 H/cm<sup>3</sup>, for spinning nano-carbons (top left) and spinning nano-silicates (bottom left). Secondly, the right panels present the predicted correlations between the mid-IR thermal emission in the IRAS 12  $\mu\text{m}$  filter and the spinning dust emission at 30 GHz. These results highlight the spinning dust intensity dispersion at 30 GHz as a function of both  $G_0$  and the local gas density  $n_{\text{H}}$ . Comparing lines of sight with the same column density but dominated by low ( $n_{\text{H}} \sim 0.1$  H/cm<sup>3</sup>), moderate ( $n_{\text{H}} \sim 30$  H/cm<sup>3</sup>), or high densities ( $n_{\text{H}} \sim 1\,000$  H/cm<sup>3</sup>), the latter being typical of translucent clouds, we see that for  $G_0 = 1$  we expect spinning dust 30 GHz intensity variations of about 2 orders of magnitude for nano-carbons, while for nano-silicates, with  $m = 0.3$  and 1 D, the intensity varies by 2 and 6 orders of magnitude, respectively. It appears that the spinning nano-carbon models spread rather evenly about the observational data point while the spinning

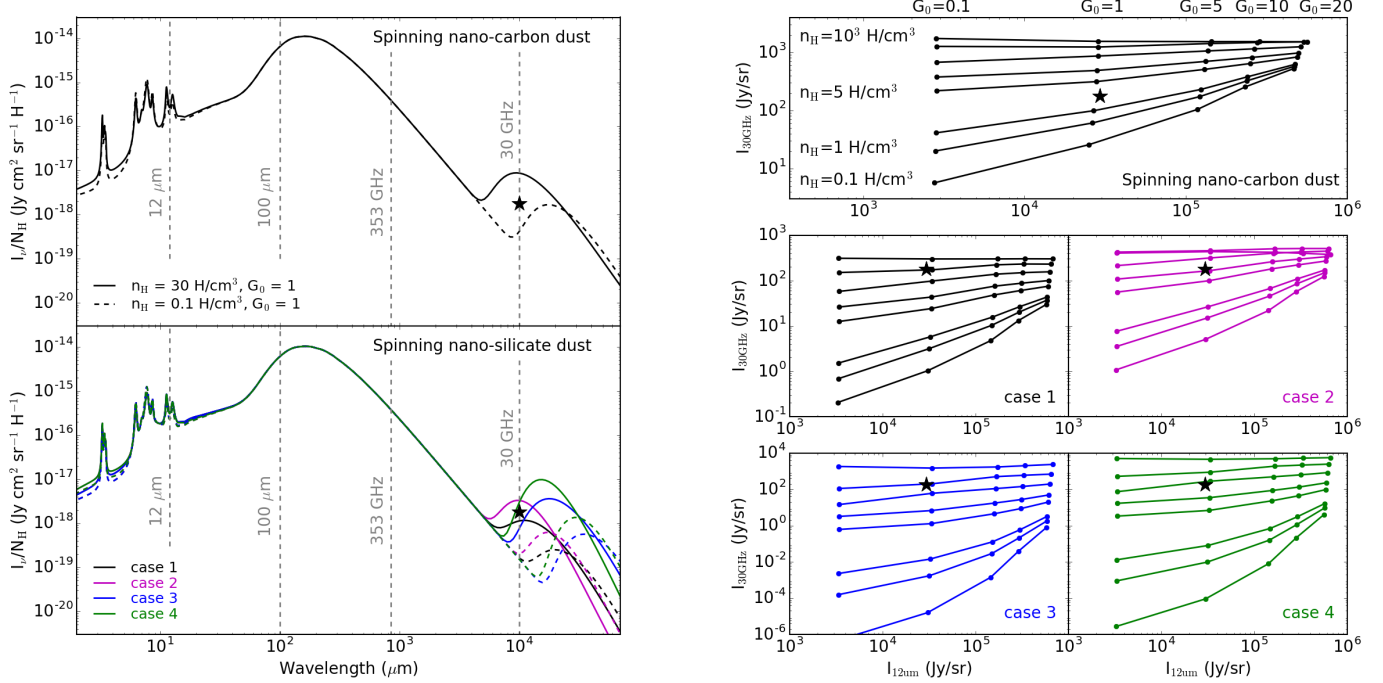


**Fig. 3.** Thermal and spinning dust modelling results. *Left:* Dust SEDs for media illuminated by the ISRF with  $G_0 = 1$ . The dashed and solid lines show the cases of media with gas local densities of  $30 \text{ H/cm}^3$  and  $0.1 \text{ H/cm}^3$ , respectively. The black star shows the average AME emissivity at 30 GHz for the bulk of pixels included in the 50% contour in Fig. 5, to avoid pixels with the highest and lowest densities and radiation fields. The upper figure shows the case of spinning nano-carbon grains and the bottom one of spinning nano-silicates with case 1 in black, case 2 in magenta, case 3 in blue and case 4 in green, see Sect. 3.1 for details. *Right:* spinning nano-dust emission at 30 GHz vs. thermal nano-dust emission at  $12 \mu\text{m}$  for  $N_{\text{HI}} = 10^{20} \text{ H/cm}^2$ . Each figure shows the results obtained for media with densities  $n_{\text{H}} = 0.1, 0.5, 1, 5, 10, 30, 100$  and  $1000 \text{ H/cm}^3$  from bottom to top and radiation fields scaled by  $G_0 = 0.1, 1, 5, 10$  and  $20$  from left to right. The upper figure displays the case of spinning nano-carbons. The lower figures show the four cases of spinning nano-silicates described in Sect. 3.1: case 1 in black, case 2 in magenta, case 3 in blue and case 4 in green. The black star shows the average AME emissivity at 30 GHz vs. the average emissivity at  $12 \mu\text{m}$ , both scaled to  $N_{\text{H}} = 10^{20} \text{ H/cm}^2$ .

nano-silicate models tend to lie below this point. We note that the  $12 \mu\text{m}$  intensity remains almost constant for all of the considered models. This implies that the poor mid-IR emission to 30 GHz AME correlation predicted from the spinning nano-carbon models must be worse from the spinning nano-silicate model. This correlation does not improve if, instead of the  $12 \mu\text{m}$  thermal emission, we consider that at  $100 \mu\text{m}$ . Therefore, the quality of the 30 GHz vs.  $12$  or  $100 \mu\text{m}$  correlation solely cannot be used to exclude any particular carrier. Then, if only the abundance of nano-carbon dust is allowed to vary (at constant size distribution and environment properties), the spinning nano-carbon dust models predict a positive correlation between  $\text{AME}_{30\text{GHz}}/N_{\text{HI}}$  and  $I_{12\mu\text{m}}/R$ , both proportional to the nano-carbon dust abundance, a correlation that is not present in the observations (see for instance Hensley et al. 2016). This lack of correlation is a strong constraint on the models that we further explore in Sect. 5. Spinning nano-silicate models predict a weaker correlation since the nano-silicates account for only  $\sim 18\%$  of the total emission in the IRAS  $12 \mu\text{m}$  band for  $G_0 = 1$ .

From the results presented in Figs. 3 and 4 we make two remarks concerning the comparison of the models with observations. Firstly, to achieve the same 30 GHz intensity, higher local densities are required for spinning nano-silicates than for nano-carbons. For example, at  $G_0 = 1$ , to obtain the same intensity as spinning nano-carbons in a medium with  $n_{\text{H}} = 5 \text{ H/cm}^3$ , the nano-silicate model requires densities of the order of 100

to  $1000 \text{ H/cm}^3$ . This difference is mainly explained by the difference in the contribution of the IR emission to the rotational excitation<sup>6</sup> of the subnanometer grains responsible for the SED of the spinning dust (left panel in Fig. 4). Thus, for the case  $n_{\text{H}} = 0.1 \text{ H/cm}^3$  and  $G_0 = 1$  presented in Fig. 4 (dashed lines), the rotational excitation by IR emission is a factor 0.8 lower and the braking 1.5 higher for a  $0.45 \text{ nm}$  nano-silicate than for a nano-carbon of the same size. These discrepancies become even larger with increasing size (factors 0.6 and 7.5, respectively, for  $0.6 \text{ nm}$  nano-grains) which explains the narrower SEDs for nano-silicates than for nano-carbons on the low frequency side (right panel in Fig. 4). These differences in both the spinning SED intensity and width imply that, if the gas distribution among the different ISM phases along a given line of sight is known, it should in principle be possible to state which types of grains are the dominant AME carriers. Then, regardless of the gas density used to model the spinning dust emission, the peak frequency and the width of the spectra differ sufficiently between spinning nano-carbons and nano-silicates that they result in significantly different  $I_{30\text{GHz}}/I_{40\text{GHz}}$  and  $I_{30\text{GHz}}/I_{20\text{GHz}}$  intensity ratios (see the example presented in Fig. 4 right panel). This indicates that several frequencies, and not just one (i.e. 30 GHz), are needed in order to characterise the AME. Correlating the 30 GHz AME

<sup>6</sup> See for instance Eqs. 95 and 106 of Silsbee et al. (2011) where it is shown that the IR excitation and damping rates are proportional to  $\int_0^\infty I_\nu/\nu^2 d\nu$  and  $\int_0^\infty I_\nu/\nu d\nu$ , respectively.

with the 20 and 40 GHz AME is therefore more discriminating than using the mid- to far-IR emission to characterise the AME carriers.

#### 4. CNM vs. WNM fraction in the diffuse neutral ISM

As shown in Sect. 3.3, unlike thermal dust emission, spinning dust emission depends not only on the radiation field but also on the gas density. The local gas properties impact the total intensity of the rotational spectrum, its peak frequency and its width. This implies that to effectively model the AME and its correlation with other observed quantities, a realistic estimate of the gas density distribution is essential.

The diffuse neutral medium, on which this study is focussed, can be described as a two-phase medium (e.g. Field et al. 1969; McKee & Ostriker 1977; Wolfire et al. 2003). At thermal equilibrium, the principal heating and cooling processes acting on the interstellar gas allow for the existence of two thermally stable HI phases distinguished by their density and temperature: a cold neutral medium (CNM) with a low kinetic temperature  $T \sim 30-200$  K and high density  $n_{\text{H}} \sim 5-120$  H/cm<sup>3</sup> and a warm neutral medium (WNM) with high temperature  $T \sim 4\,100-8\,800$  K and low density  $n_{\text{H}} \sim 0.03-1.3$  H/cm<sup>3</sup>. The existence of these two phases has been confirmed observationally (e.g. Liszt et al. 1993; Heiles & Troland 2003; Nguyen et al. 2019; Murray et al. 2020, among others). However, it has been shown that a significant fraction of the WNM is actually cooler than expected ( $T \sim 500-5\,000$  K), and thus falls into the thermally unstable regime, but the exact proportion of this unstable HI is still debated (e.g. Heiles & Troland 2003; Murray et al. 2018).

Observations show that the CNM fraction,  $f_{\text{CNM}} = N_{\text{HI}}^{\text{CNM}} / (N_{\text{HI}}^{\text{CNM}} + N_{\text{HI}}^{\text{WNM}})$ , increases with the total column density of HI and also in the surroundings of molecular clouds (e.g. Stanimirović et al. 2014). For very diffuse high latitude sightlines, with HI column densities ranging from  $3 \times 10^{16}$  to a few  $10^{21}$  cm<sup>2</sup>, Murray et al. (2015) found that  $f_{\text{CNM}}$  ranges from less than 0.1 to 0.51 with a median value of 0.20. This agrees with the median  $f_{\text{CNM}} = 0.23$  measured by Heiles & Troland (2003) for sightlines with  $|b| > 10^\circ$  and  $N_{\text{HI}}$  from a few  $10^{20}$  to a few  $10^{21}$  H/cm<sup>2</sup>. Stanimirović et al. (2014) further showed that for column densities from  $\sim 10^{18}$  to a few  $10^{21}$  H/cm<sup>2</sup>, the HI column density of the WNM is relatively uniform whereas at  $N_{\text{HI}} \sim 10^{21}$  H/cm<sup>2</sup> the CNM fraction increases from almost negligible to  $\sim 40\%$  around Perseus with a median value of 33%. Regions such as Perseus are representative of the areas selected for our study (Fig. 1) and it is indeed included in the mask defined in Sect. 2.4 as are the Taurus and Gemini regions for which Nguyen et al. (2019) found  $f_{\text{CNM}} = 37\%$  and 16%, respectively. Similar results were found in the California, Rosette, MonOB1 and NGC2264 regions (Nguyen et al. 2019) which are also included in our mask.

Of the sightlines included in our study 92% have  $5 \times 10^{20} \leq N_{\text{HI}} \leq 5 \times 10^{21}$  H/cm<sup>2</sup> and are above the Galactic Plane. In the following, we therefore make the reasonable assumption that, in order to model AME by spinning nano-dust emission, a model is acceptable only if it uses a mixture of CNM and WNM with  $0.05 \leq f_{\text{CNM}} \leq 0.4$  and if it matches the AME and mid-IR brightness for HI column densities matching the distribution shown in Fig. 2.

#### 5. Modelling results

To test the different models, we consider CNM/WNM mixtures with  $f_{\text{CNM}} = 0$  to 0.5 in steps of 0.05 illuminated by the Mathis

et al. (1983) radiation field<sup>7</sup> with  $G_0 = 1$ . The HI column density is set equal to the median, the mean or the mode of the  $N_{\text{HI}}$  distribution (see Fig. 2). A model is considered acceptable if it is found within the contour encompassing 75% of the pixels, simultaneously, for all three of the ratios  $\text{AME}_{30\text{ GHz}}$  vs.  $\text{AME}_{20\text{ GHz}}$ ,  $\text{AME}_{30\text{ GHz}}$  vs.  $\text{AME}_{40\text{ GHz}}$  and  $\text{AME}_{30\text{ GHz}}$  vs. dust emission in the IRAS 12  $\mu\text{m}$  filter, for at least one of the tested column densities. All models are run for both nano-carbons and nano-silicates with the properties described in Sect. 3.1. Figures 5 and 6 show the results.

##### 5.1. Digression on observation correlations

Before going into the details of the modelling, we explore the level of correlation between the different data sets (Fig. 5). Thanks to the new treatment applied to the IRAS data (see Appendix A), excluding the noisiest areas (see Sect. 2.4), we see that for an angular resolution of  $1^\circ$  the strength of the linear correlation of the AME is as good with the emission at 12  $\mu\text{m}$  as with that at 100  $\mu\text{m}$ : Pearson correlation coefficients of  $r_P = 0.96$  and 0.94, respectively. As expected, matter correlates with matter, which shows that our results will not be limited by data problems but simply by our level of understanding of the dust. As can be seen in Fig. 5 the data dispersion remains relatively high, which needs to be explained either by different environments (our mask includes 24% of the sky) or by variations in the nano-grain properties (nature, size distribution, abundance, electric dipole moment). If suitable matches between the models and the data are not possible, then the spinning nano-grain hypothesis will have to be discarded.

##### 5.2. Spinning nano-carbon dust

The spinning nano-carbon grain model is able to reproduce the observed trends in Fig. 5 (black symbols), but these results do not allow us to constrain the density of the WNM because all of the tested values,  $0.05 \leq n_{\text{H}}^{\text{WNM}} \leq 1$  H/cm<sup>3</sup>, yield solutions for pixels within both the 75% and 50% contours. However, we do note two interesting results. Firstly, the CNM density depends on the WNM density and a denser WNM implies a denser CNM. For example, for models with a  $n_{\text{H}}^{\text{WNM}} = 0.1$  H/cm<sup>3</sup>, the CNM density must be between 20 and 40 H/cm<sup>3</sup>. Whereas, if  $n_{\text{H}}^{\text{WNM}} = 0.6$  H/cm<sup>3</sup>,  $n_{\text{H}}^{\text{CNM}}$  must be between 30 and 60 H/cm<sup>3</sup>, and if  $n_{\text{H}}^{\text{WNM}} = 1$  H/cm<sup>3</sup>, then  $n_{\text{H}}^{\text{CNM}}$  must be between 40 and 100 H/cm<sup>3</sup>. Secondly, all viable models require  $0.1 \leq f_{\text{CNM}} \leq 0.2$ , which is in agreement with the observational studies cited in Sect. 4. This is also in agreement with the results of Ysard et al. (2010) who used the IRIS map at 12  $\mu\text{m}$  and the 23 GHz AME map derived by Miville-Deschénes et al. (2008) from WMAP data to study 27 regions of a few square degrees, all included in our mask. With a spinning PAH model, they obtained  $f_{\text{CNM}} \sim 10\%$  for all regions and  $m \sim 0.4$  D for most of them. This is a good indication that models using carbonaceous nano-grains, regardless of their exact nature, give comparable results.

The grain electric dipole moment is probably the most uncertain dust parameter in our modelling, and so we also show the results for the same nano-carbon dust but with a higher dipole moment of  $m = 0.5$  D (pink symbols in Fig. 5). The spinning nano-carbon grain results still hold but the required density of the WNM for the models that fit cannot exceed 0.7 H/cm<sup>3</sup>. With

<sup>7</sup> According to Fanciullo et al. (2015), the typical  $G_0$  variations range from  $\sim 0.8$  to 1.4.

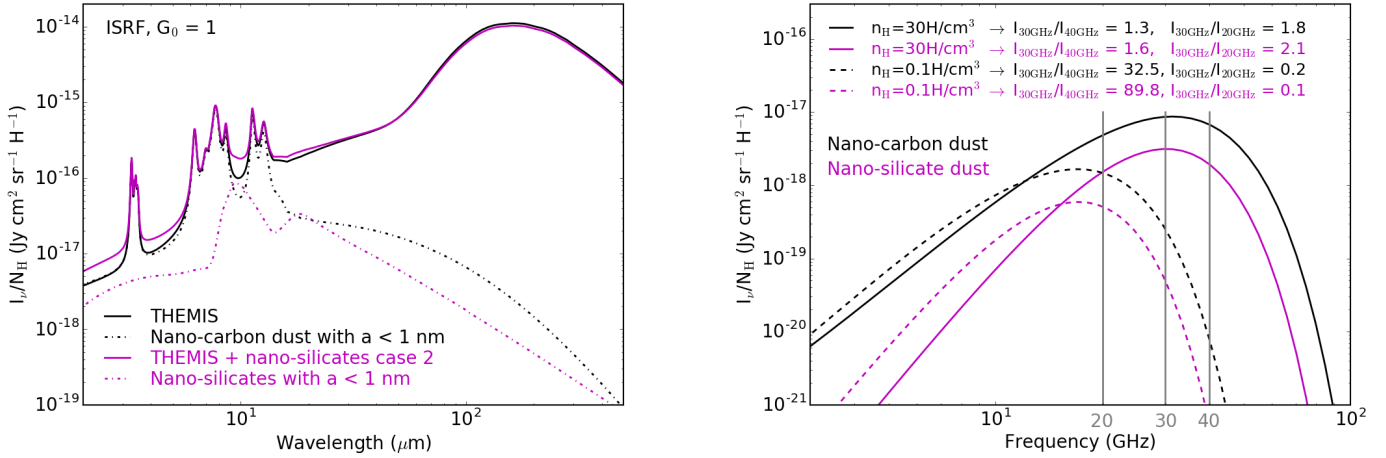


**Fig. 4.** *Left:* SED of thermal dust emission for dust models without (black lines) and with (magenta lines) nano-silicate dust, for  $G_0 = 1$ . In both cases, the dash-dotted lines show the contribution of the smallest nano-grains with  $a < 1 \text{ nm}$  responsible for the spinning dust emission. The nano-silicates are those of case 2 which are the closest in both size distribution and electric dipole moment to THEMIS nano-carbon dust. *Right:* corresponding spinning dust emission for media with  $n_{\text{H}} = 0.1$  and  $30 \text{ H/cm}^3$ , solid and dashed lines respectively.

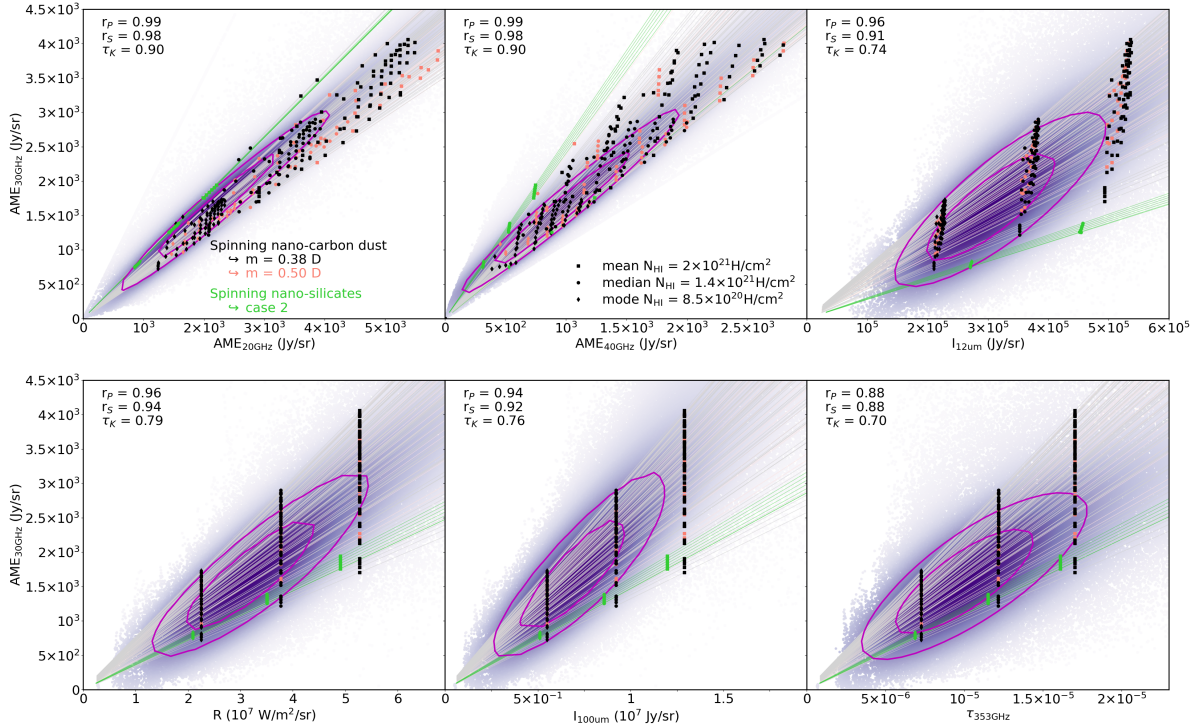


**Fig. 5.** Top from left to right: observations are plotted as density of points maps of AME<sub>30 GHz</sub> vs. AME<sub>20 GHz</sub>, vs. AME<sub>40 GHz</sub> and vs. dust emission in the 12  $\mu\text{m}$  IRAS filter. Bottom from left to right: observations are plotted as density of points maps of AME<sub>30 GHz</sub> vs. radiance, vs. dust emission in the 100  $\mu\text{m}$  IRAS filter and vs. optical depth at 353 GHz. For all figures, overplotted are the contours enclosing 50% of the pixels (internal one) and 75% of the pixels (external one). The models fitting the observations are shown with black and pink symbols for spinning nano-carbon dust,  $m = 0.38$  and  $0.5 \text{ D}$  respectively, and green symbols for spinning nano-silicate dust (case 2, see Sect. 5 for details). Squares, circles and diamonds show models scaled to the mean ( $N_{\text{HI}} = 2 \times 10^{21} \text{ H/cm}^2$ ), the median ( $N_{\text{HI}} = 1.4 \times 10^{21} \text{ H/cm}^2$ ) and the mode HI column density ( $N_{\text{HI}} = 8.5 \times 10^{20} \text{ H/cm}^2$ ), respectively. The light grey, pink and green lines show the same models for HI column densities extending over the entire observational range  $10^{20} \leq N_{\text{HI}} \leq 1.4 \times 10^{22} \text{ H/cm}^2$ . The various model points show spinning dust models for different  $f_{\text{CNM}}$  values (see Sect. 5.2 for details). The  $r_P$ ,  $r_S$  and  $\tau_K$  give the Pearson correlation coefficient, the Spearman rank-order correlation coefficient and the Kendall's tau, respectively.

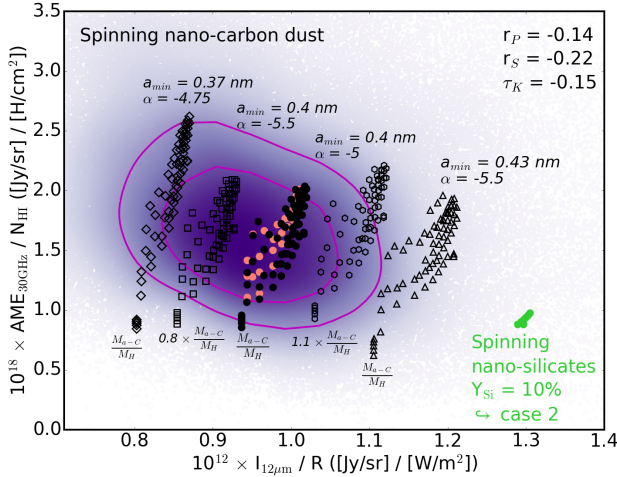


**Fig. 6.** Density of points map of  $\text{AME}_{30 \text{ GHz}}/\text{N}_{\text{HI}}$  vs.  $I_{12\mu\text{m}}/R$ . Overplotted are the contours enclosing 50% of the pixels (internal one) and 75% of the pixels (external one). The  $r_P$ ,  $r_S$  and  $\tau_K$  give the corresponding Pearson correlation coefficient, the Spearman rank-order correlation coefficient and the Kendall's tau, respectively. The same models as in Fig. 5 are shown with black and pink circles for spinning nano-carbon dust,  $m = 0.38$  and  $0.5$  D respectively, and green circles for spinning nano-silicate dust (case 2), each symbol showing a different value of  $f_{\text{CNM}}$  (see Sects. 5.2 and 5.3 for details). For spinning nano-carbon dust we show models with the same  $f_{\text{CNM}}$  but with variations in the size distribution and dust abundance. The standard THEMIS size distribution with  $a_{\min} = 0.4 \text{ nm}$  and  $\alpha = -5$ , where  $\alpha$  is the a-C nano-particle power law exponent, is shown for  $m = 0.38$  D (black circles). We show this same model but with an abundance increase of 10% (hexagons). The squares are for  $a_{\min} = 0.4 \text{ nm}$ ,  $\alpha = -5.5$  and an abundance decrease by 20%. The triangles for  $a_{\min} = 0.43 \text{ nm}$  and  $\alpha = -5.5$ , and the diamonds for  $a_{\min} = 0.37 \text{ nm}$  and  $\alpha = -4.75$  with the standard model abundances.

a higher electric dipole moment, the spinning nano-carbon spectrum shifts to the lower frequency, WNM-dominated side. In order to not overestimate the intensity at 20 GHz, the rotational excitation by the gas in the WNM must be lower, which requires a lower gas density.

For consistency, we also show the  $\text{AME}_{30 \text{ GHz}}$  correlation with the radiance (proportional to the radiation field and the column density), the intensity in the IRAS 100  $\mu\text{m}$  band (emission from big grains at thermal equilibrium) and the dust opacity at 353 GHz. All models that are in accordance with the AME and the mid-IR emission are also in agreement with these far-IR/submm emission (derived) observations, illustrating the consistency of THEMIS at all wavelengths.

Figure 6 shows  $\text{AME}_{30 \text{ GHz}}/\text{N}_{\text{HI}}$  as a function of  $I_{12\mu\text{m}}/R$ . Assuming that there is no nano-silicate dust in the diffuse ISM,  $I_{12\mu\text{m}}/R$  is proportional to the nano-carbon dust abundance. According to Fanciullo et al. (2015), the typical  $G_0$  variations range from  $\sim 0.8$  to  $1.4$  in the diffuse ISM, which leads to variations in  $\text{AME}_{30 \text{ GHz}}/\text{N}_{\text{HI}}$  of  $\sim -4$  to  $+8\%$  for the CNM/WNM mixtures required by the viable spinning dust models shown in Fig. 5. The models that best account for the observations presented so far are also in agreement with the correlations in the ratios (full black and pink dots in Fig. 6 for  $m = 0.38$  and  $0.5$  D, respectively). If it is indeed due to spinning dust, the

$\text{AME}_{30 \text{ GHz}}/\text{N}_{\text{HI}}$  ratio should be roughly proportional to the nano-carbon dust abundance. There is no obvious correlation in the data with a Pearson correlation coefficient of  $-0.14$ . On the one hand, this is perhaps an illustration of the fact that the excitation of the rotation of nano-grains depends on interactions with the gas and also on the UV radiation field, whereas the mid-IR emission depends only on the latter. On the other hand, the observed dispersion could be the result of little variations in the nano-grain size distribution. Nano-carbon grains, whether PAHs or amorphous hydrocarbons, are the dust population that is the most affected by stellar photo-processing and shock waves, both leading to variations in their size distribution and abundance (e.g. Bocchio et al. 2014; Murga et al. 2019; Murga 2020; Joblin et al. 2020; Schirmer et al. 2020). Indeed, the observed dispersion in the correlations of the ratios can be explained by small variations the size distribution and abundance (black symbols in Fig. 6). Photo-processing studies show that a decrease in the nano-grain abundance is also associated with a change in the size distribution. For example, Schirmer et al. (2020) showed that in the Horsehead Nebula the slope of the nano-carbon dust size distribution steepens from  $n(a) \propto a^{-5}$  to  $n(a) \propto a^{-5.5}$  to  $-7.5$ . Considering the least extreme case,  $n(a) \propto a^{-5.5}$  and a 20% decrease in the grain abundance, we obtain the squares in Fig. 6. Our results also show that a slight increase in the nano-carbon dust abundance (hexagons), a small increase in the minimum size coupled to a steeper size distribution slope (triangles), or a shallower size distribution coupled to a smaller minimum size (diamonds) can explain the observed dispersion. The minimum size and slope of the size distribution are indeed degenerate as they both control the quantity of the smallest nano-grains which are responsible for the AME. These models are also consistent with the correlations presented in Fig. 5.

### 5.3. Spinning nano-silicate dust

For the spinning nano-silicates with the highest electric dipole moment (cases 3 and 4,  $m = 1$  D), we find that it is impossible to simultaneously fit the  $\text{AME}_{30 \text{ GHz}}$  vs.  $\text{AME}_{20 \text{ GHz}}$  and  $\text{AME}_{30 \text{ GHz}}$  vs.  $\text{AME}_{40 \text{ GHz}}$  ratios. This electric dipole moment is indeed high enough to significantly slow down the rotation speed and thus leads to spinning emission peaking at lower frequencies than observed. This implies that even if it is possible to reproduce the intensity level at a single given frequency, for instance at 30 GHz, the spectral shape will be incorrect and so the required intensities at the two other frequencies cannot be retrieved. We note that the quantum mechanical calculations performed by Macià Escatllar & Bromley (2020) and Mariñoso Guiu et al. (2021) show that Mg-rich nano-silicates will always have  $m > 1$  D, even when covered by an ice layer. However, such large dipole moments for nano-silicates appear to be inconsistent with the observations (see also Hoang et al. 2016; Hensley & Draine 2017).

Only nano-silicates with a lower dipole moment and a size distribution centred on the smallest grains give spinning emission within the 75% contour (case 2:  $m = 0.3$  D and  $\sigma = 0.1$ , green symbols in Fig. 5). However, this works for only 6 CNM/WNM mixtures, all having  $f_{\text{CNM}} = 0.3$  and a CNM density  $n_{\text{H}} = 20 \text{ H/cm}^3$ , with the WNM density varying from  $0.5$  to  $1 \text{ H/cm}^3$ . The reason why so few models fall within the 75% contour is that the intensity in the IRAS 12  $\mu\text{m}$  band is too high. This is more obvious when we plot the  $\text{AME}_{30 \text{ GHz}}/\text{N}_{\text{HI}}$  ratio over  $I_{12\mu\text{m}}/R$  for which the nano-silicates are within the observed dispersion but not within the 75% contour (green dots in Fig. 6). This leads us to the following conclusion: if  $Y_{\text{Si}} = 10\%$ , then

nano-silicates can only marginally contribute to the AME, whatever their properties.

The only way to reduce the nano-silicate mid-IR emission is to decrease  $Y_{\text{Si}}$ . However, for  $G_0 = 1$ , the nano-silicates only account for about 18% of the total intensity because the IRAS 12  $\mu\text{m}$  filter is very wide ( $\sim 7 \mu\text{m}$ ) – they do, however, account for 45% of the total intensity at the peak frequency of the relatively narrow, silicate spectral feature at 9.8  $\mu\text{m}$ . As a result, halving  $Y_{\text{Si}}$ , only decreases  $I_{12\mu\text{m}}$  by about 9% while the 30 GHz spinning emission is decreased by 50%. We therefore come to the same conclusion, that nano-silicates can, at best, only contribute marginally to the observed AME.

Hensley & Draine (2017) suggested that uncertainties in the grain equilibrium charge distribution could lead to uncertainty in the nano-silicate spinning SED, in particular if the amount of negatively charged grains is underestimated, these being indeed more rotationally excited. As discussed in Weingartner & Draine (2001), the grain charge distribution and the amount of negatively charged grains depends on the bulk work function  $W$  which we take to be 4.97 eV for silicates following Kimura (2016, and references therein) instead of 8 eV, a standard value adopted for all grains, carbon or silicate based (Draine 1978). To test the influence of this choice, we ran calculations with  $W = 8$  eV. Using the same fitting procedure, our results are barely changed: only case 2 nano-silicates give a few models within the 75% contour, for the same CNM and WNM gas densities, the only difference being that  $f_{\text{CNM}}$  is decreased to 0.25. This is actually a consequence of the fact that negatively charged grains are not abundant in the UV pervaded diffuse gas.

Are the above conclusions biased because THEMIS comprises amorphous aromatic-rich nano-carbon grains rather than ‘astro-PAHs’? The answer is no. If we take the PAHs of the Compiègne et al. (2011) model, in the IRAS 12  $\mu\text{m}$  band the difference is only  $\sim 3\%$  in favour of THEMIS. Could the difference come from the adopted silicate optical properties? Once again the answer is no. Comparison with the Draine & Li (2007) model, which contains both PAHs and nano-silicates, in more or less the same proportions as our case 2, at  $G_0 = 1$  the difference in the IRAS 12  $\mu\text{m}$  band is  $\sim 5\%$ , again in favour of THEMIS. This means that for the considered diffuse ISM sky area (Fig. 1), all models that attempt to explain the AME, at several frequencies, with *only* nano-silicates will have the same problem, whether using PAHs or amorphous nano-carbon grains. Hoang et al. (2016) did not have this problem because they did not consider the mid-IR emission, they tested their model against the UV extinction, polarisation of starlight and the polarisation of the AME. They were able to put constraints on both  $Y_{\text{Si}} \leq 10\%$  and  $m \geq 0.4$  D (see their Fig. 8). With regard to the results of Hensley et al. (2016),  $4 \leq Y_{\text{Si}} \leq 15\%$  and  $0.3 \leq m \leq 1$  D, we believe that the difference comes down to a single aspect: the normalisation of their spectra. Their mid-IR spectrum is that of the DCld 300.2-16.9 translucent cloud. According to Ingalls et al. (2011, and references therein), DCld 300.2-16.9 is a CNM cloud illuminated by the ISRF with  $G_0 = 1$ , with a column density of  $\sim 4 \times 10^{21} \text{ H/cm}^2$ , which was affected by supernova explosions from the Sco-Cen OB association about  $(2\text{-}6) \times 10^5$  years ago. This spectrum was scaled to the HI-correlated dust emission in the DIRBE bands as in Dwek et al. (1997):  $I_{12\mu\text{m}} = 3.16 \times 10^{-16} \text{ Jy cm}^2/\text{sr}/\text{H}$  and then associated with the median AME Planck COMMANDER spectrum normalised to  $3 \times 10^{-18} \text{ Jy cm}^2/\text{sr}/\text{H}$  at 30 GHz, which is far from the the bulk of the pixels of the intermediate latitude regions that we study here.

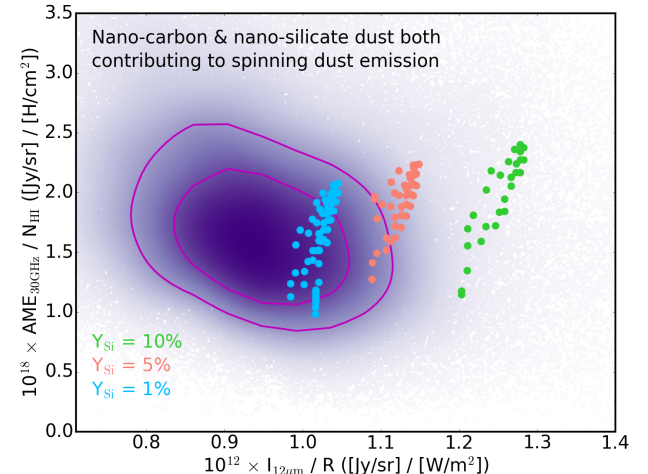


**Fig. 7.**  $\text{AME}_{30 \text{ GHz}} / N_{\text{HI}}$  vs.  $I_{12\mu\text{m}} / R$  as in Fig. 6. The green dots show best fitting models in which both the nano-carbon dust and the nano-silicate dust produce spinning emission (case 2,  $Y_{\text{Si}} = 10\%$ ,  $m = 0.3$  D,  $\sigma = 0.1$ ), with each point showing a different  $f_{\text{CNM}}$  value. Model calculations for lower abundances of nano-silicates are shown:  $Y_{\text{Si}} = 5\%$  (pink dots) and  $Y_{\text{Si}} = 1\%$  (blue dots).

#### 5.4. Combined nano-carbon and nano-silicate dust emission

If nano-carbon and nano-silicate dust co-exist in the diffuse ISM, it is reasonable to assume that both will produce spinning dust emission. For carbonaceous nano-dust we have clear and abundant observational evidence for their existence in non-negligible quantities in the ISM, while the case is not so clear-cut for nano-silicates. In order to be comprehensive we therefore repeat the fitting procedure with the assumption that both populations contribute to the AME. We do this for several values of  $Y_{\text{Si}}$  ( $= 10, 5$  and  $1\%$ ) for case 2 nano-silicates ( $m = 0.3$  D and  $\sigma = 0.1$ ). All of these nano-silicate abundances lead to acceptable CNM/WNM mixtures and we show the corresponding model results in Fig. 7. The default value  $Y_{\text{Si}} = 10\%$  is within the dispersion but does not fall within the contours surrounding the bulk of the pixels. If the abundance of nano-silicates is halved, then the models are at the edge of the 75% contour. By further lowering the abundance to  $Y_{\text{Si}} = 1\%$ , the models fall within the 50% contour, but remain on the high  $I_{12\mu\text{m}} / R$  side<sup>8</sup> and nano-silicates account only for 3 to 5% of the AME at 30 GHz depending on the CNM/WNM mixture.

What Fig. 7 indicates is that: (1) if both nano-grain populations co-exist in the diffuse ISM, then the AME must come predominantly from nano-carbon dust emission and (2) if both populations have non-zero permanent electric dipole moments then, the abundance of nano-silicates cannot exceed  $\sim 1\%$ . An upper limit that is in agreement with the findings of Désert et al. (1986), Macià Escatllar & Bromley (2020) and Mariñoso Guiu et al. (2021), all three of these studies derive an upper limit of  $Y_{\text{Si}} = 1\%$ . This is smaller than the upper limit of  $\sim 10\%$  found by Li & Draine (2001). The difference most probably comes from

<sup>8</sup> We do not show cases 1, 3 and 4 since the discrepancy comes mainly from the  $I_{12\mu\text{m}} / R$ . Indeed, case 2 and case 4 have the exact same  $I_{12\mu\text{m}} / R$ , which does not depend on  $m$  but just on  $\sigma$ . Case 1 and 3 are similar and have the same radiance (no changes in the bigger grain populations) and  $I_{12\mu\text{m}}$  values varying by no more than 2% when compared to cases 2 and 4.

the line of sight chosen by Li & Draine (2001) to test their model ( $l = 44^\circ 20'$ ,  $b = -0^\circ 20'$ ), which is in the Galactic plane and has a relatively high column density ( $N_{\text{H}} = 4.3 \times 10^{22} \text{ H/cm}^2$ ) and a radiation field with  $G_0 = 2$ . This line of sight is therefore not representative of the bulk of the diffuse ISM lines of sight at intermediate latitudes.

## 6. Conclusion

Using The Heterogeneous dust Evolution Model for Interstellar Solids (THEMIS, Jones et al. 2017), we investigated whether the nature of the grains at the origin of the AME measured by the Planck Collaboration (Planck Collaboration et al. 2016b) in the Galactic diffuse ISM can be identified. Model grids were created with the DustEM numerical tool (Compiègne et al. 2011) and compared with observations and parameters derived from them, from the mid-IR to the microwave. Our results are the following.

First, nano-carbon dust can explain all the observations for medium properties in agreement with the latest findings about the separation of CNM and WNM in the diffuse ISM. The dispersion in the observations can be accounted for with little variations in the dust size distribution, abundance or electric dipole moment. Second, whatever the properties and the abundance of the nano-silicate dust considered, spinning nano-silicates are formally excluded as being the sole source of the AME. Third, the best agreement with the observations is obtained if the emission of spinning nano-carbons *alone* is taken into account. The addition of a nano-silicate component takes the model out of the maximum density area of the correlation plots. However, a marginal participation of these nano-silicates to the AME production cannot be excluded as long as their abundance does not exceed  $Y_{\text{Si}} \sim 1\%$ .

Our results reconcile the large- and small-scale studies, where careful investigations of the carrier nature and evolution, both through modelling and data correlations, have linked AME and spinning nano-carbonaceous dust, be they amorphous hydrocarbons or PAHs. The AME is thus very promising for tracing the evolution of carbonaceous grains since the spinning emission does not only depend on the grain properties, but also on the properties of the very local medium. This should allow to test in a very constraining way the models of grain evolution, be it due to UV photons or shocks.

**Acknowledgements.** We thank our anonymous referee whose careful reading and interesting comments helped to clarify and improve the paper. This work was supported by the Programme National PCMI of CNRS/INSU with INC/INP co-funded by CEA and CNES.

## References

Abergel, A., Boulanger, F., Delouis, J. M., Dudziak, G., & Steindling, S. 1996, A&A, 309, 245

Ali-Haïmoud, Y., Hirata, C. M., & Dickinson, C. 2009, MNRAS, 395, 1055

AMI Consortium: Scaife, A. M. M., Green, D. A., Pooley, G. G., et al. 2010, MNRAS, 403, L46

Arab, H., Abergel, A., Habart, E., et al. 2012, A&A, 541, A19

Bell, A. C., Onaka, T., Galliano, F., et al. 2019, PASJ, 71, 123

Bennett, C. L., Larson, D., Weiland, J. L., et al. 2013, ApJS, 208, 20

Bernard, J. P., Abergel, A., Ristorcelli, I., et al. 1999, A&A, 347, 640

Berné, O., Joblin, C., Deville, Y., et al. 2007, A&A, 469, 575

Bocchio, M., Jones, A. P., & Slavin, J. D. 2014, A&A, 570, A32

Campeggio, L., Strafella, F., Maiolo, B., Elia, D., & Aiello, S. 2007, ApJ, 668, 316

Casassus, S., Dickinson, C., Cleary, K., et al. 2008, MNRAS, 391, 1075

Casassus, S., Vidal, M., Arce-Tord, C., et al. 2021, MNRAS, 502, 589

Cepeda-Arroita, R., Harper, S. E., Dickinson, C., et al. 2021, MNRAS, 503, 2927

Compiègne, M., Abergel, A., Verstraete, L., & Habart, E. 2008, A&A, 491, 797

Compiègne, M., Verstraete, L., Jones, A., et al. 2011, A&A, 525, A103

Désert, F. X., Boulanger, F., Leger, A., Puget, J. L., & Sellgren, K. 1986, A&A, 159, 328

Dickinson, C., Ali-Haïmoud, Y., Barr, A., et al. 2018, New A Rev., 80, 1

Draine, B. T. 1978, ApJS, 36, 595

Draine, B. T. & Hensley, B. 2013, ApJ, 765, 159

Draine, B. T. & Lazarian, A. 1998a, ApJ, 508, 157

Draine, B. T. & Lazarian, A. 1998b, ApJ, 508, 157

Draine, B. T. & Lazarian, A. 1999, ApJ, 512, 740

Draine, B. T. & Li, A. 2007, ApJ, 657, 810

Dwek, E., Arendt, R. G., Fixsen, D. J., et al. 1997, ApJ, 475, 565

Fanciullo, L., Guillet, V., Aniano, G., et al. 2015, A&A, 580, A136

Fanciullo, L., Guillet, V., Boulanger, F., & Jones, A. P. 2017, A&A, 602, A7

Ferland, G. J., Korista, K. T., Verner, D. A., et al. 1998, PASP, 110, 761

Field, G. B., Goldsmith, D. W., & Habing, H. J. 1969, ApJ, 155, L149

Flagey, N., Noriega-Crespo, A., Boulanger, F., et al. 2009, ApJ, 701, 1450

Górski, K. M., Hivon, E., Banday, A. J., et al. 2005, ApJ, 622, 759

Guhathakurta, P. & Draine, B. T. 1989, ApJ, 345, 230

Harper, S. E., Dickinson, C., & Cleary, K. 2015, MNRAS, 453, 3375

Haslam, C. G. T., Salter, C. J., Stoffel, H., & Wilson, W. E. 1982, A&AS, 47, 1

Heiles, C. & Troland, T. H. 2003, ApJ, 586, 1067

Hensley, B. S. & Draine, B. T. 2017, ApJ, 836, 179

Hensley, B. S., Draine, B. T., & Meissner, A. M. 2016, ApJ, 827, 45

HI4PI Collaboration, Ben Bekhti, N., Flöer, L., et al. 2016, A&A, 594, A116

Hoang, T. & Lazarian, A. 2016, ApJ, 821, 91

Hoang, T., Vinh, N.-A., & Quynh Lan, N. 2016, ApJ, 824, 18

Ingalls, J. G., Bania, T. M., Boulanger, F., et al. 2011, ApJ, 743, 174

Joblin, C., Wenzel, G., Rodriguez Castillo, S., et al. 2020, in Journal of Physics Conference Series, Vol. 1412, Journal of Physics Conference Series, 062002

Jones, A. P. 2009, A&A, 506, 797

Jones, A. P. 2012a, A&A, 540, A1

Jones, A. P. 2012b, A&A, 540, A2

Jones, A. P. 2012c, A&A, 542, A98

Jones, A. P., Fanciullo, L., Köhler, M., et al. 2013, A&A, 558, A62

Jones, A. P., Köhler, M., Ysard, N., Bocchio, M., & Verstraete, L. 2017, A&A, 602, A46

Jones, A. P., Ysard, N., Köhler, M., et al. 2014, Faraday Discussions, 168, 313

Juvela, M., Neha, S., Mannfors, E., et al. 2020, A&A, 643, A132

Kelsall, T., Weiland, J. L., Franz, B. A., et al. 1998, ApJ, 508, 44

Kim, S.-H., Martin, P. G., & Hendry, P. D. 1994, ApJ, 422, 164

Kimura, H. 2016, MNRAS, 459, 2751

Kogut, A., Banday, A. J., Bennett, C. L., et al. 1996, ApJ, 460, 1

Köhler, M., Stepnik, B., Jones, A. P., et al. 2012, A&A, 548, A61

Köhler, M., Ysard, N., & Jones, A. P. 2015, A&A, 579, A15

Laureijs, R. J., Clark, F. O., & Prusti, T. 1991, ApJ, 372, 185

Lefèvre, C., Pagani, L., Juvela, M., et al. 2014, A&A, 572, A20

Leitch, E. M., Readhead, A. C. S., Pearson, T. J., & Myers, S. T. 1997, ApJ, 486, L23

Li, A. & Draine, B. T. 2001, ApJ, 550, L213

Liszt, H. S., Braun, R., & Greisen, E. W. 1993, AJ, 106, 2349

Macià Escatllar, A. & Bromley, S. T. 2020, A&A, 634, A77

Mariño Guiu, J., Ferrero, S., Macià Escatllar, A., Rimola, A., & Bromley, S. T. 2021, Frontiers in Astronomy and Space Sciences, 8, 80

Mathis, J. S., Mezger, P. G., & Panagia, N. 1983, A&A, 128, 212

Mathis, J. S. & Whiffen, G. 1989, ApJ, 341, 808

McKee, C. F. & Ostriker, J. P. 1977, ApJ, 218, 148

Miville-Deschénes, M.-A. & Lagache, G. 2005, ApJS, 157, 302

Miville-Deschénes, M. A., Ysard, N., Lavabre, A., et al. 2008, A&A, 490, 1093

Murga, M. S. 2020, INASAN Science Reports, 5, 298

Murga, M. S., Khoperskov, S. A., & Wiebe, D. S. 2016, Astronomy Reports, 60, 669

Murga, M. S., Wiebe, D. S., Sivkova, E. E., & Akimkin, V. V. 2019, MNRAS, 488, 965

Murray, C. E., Peek, J. E. G., & Kim, C.-G. 2020, ApJ, 899, 15

Murray, C. E., Stanimirović, S., Goss, W. M., et al. 2015, ApJ, 804, 89

Murray, C. E., Stanimirović, S., Goss, W. M., et al. 2018, ApJS, 238, 14

Nashimoto, M., Hattori, M., Poidevin, F., & Génova-Santos, R. 2020, ApJ, 900, L40

Nguyen, H., Dawson, J. R., Lee, M.-Y., et al. 2019, ApJ, 880, 141

Ormel, C. W., Paszun, D., Dominik, C., & Tielens, A. G. G. M. 2009, A&A, 502, 845

Pilleri, P., Montillaud, J., Berné, O., & Joblin, C. 2012, A&A, 542, A69

Pilleri, P., Reisenfeld, D. B., Zurbuchen, T. H., et al. 2015, ApJ, 812, 1

Planck Collaboration, Abergel, A., Ade, P. A. R., et al. 2014a, A&A, 571, A11

Planck Collaboration, Adam, R., Ade, P. A. R., et al. 2016a, A&A, 594, A1

Planck Collaboration, Adam, R., Ade, P. A. R., et al. 2016b, A&A, 594, A10

Planck Collaboration, Ade, P. A. R., Aghanim, N., et al. 2016c, A&A, 594, A25

Planck Collaboration, Ade, P. A. R., Aghanim, N., et al. 2014b, A&A, 565, A103

Ridderstad, M., Juvela, M., Lehtinen, K., Lemke, D., & Liljeström, T. 2006, *A&A*, 451, 961

Saajasto, M., Juvela, M., Lefèvre, C., Pagani, L., & Ysard, N. 2021, *A&A*, 647, A109

Schirmer, T., Abergel, A., Verstraete, L., et al. 2020, *A&A*, 639, A144

Schlegel, D. J., Finkbeiner, D. P., & Davis, M. 1998, *ApJ*, 500, 525

Silsbee, K., Ali-Haïmoud, Y., & Hirata, C. M. 2011, *MNRAS*, 411, 2750

Stanimirović, S., Murray, C. E., Lee, M.-Y., Heiles, C., & Miller, J. 2014, *ApJ*, 793, 132

Stepnik, B., Abergel, A., Bernard, J. P., et al. 2003, *A&A*, 398, 551

Tibbs, C. T., Flagey, N., Paladini, R., et al. 2011, *MNRAS*, 418, 1889

Tibbs, C. T., Watson, R. A., Dickinson, C., et al. 2010, *MNRAS*, 402, 1969

Vaillancourt, J. E., Andersson, B. G., Clemens, D. P., et al. 2020, *ApJ*, 905, 157

Vidal, M., Dickinson, C., Harper, S. E., Casassus, S., & Witt, A. N. 2020, *MNRAS*, 495, 1122

Weingartner, J. C. & Draine, B. T. 2001, *ApJS*, 134, 263

Wheelock, S., Gautier, T. N., Chillemi, J., et al. 1993, ISSA Explanatory Supplement, Tech. rep., Page:

Wheelock, S. L., Gautier, T. N., Chillemi, J., et al. 1994, IRAS sky survey atlas: Explanatory supplement, NASA STI/Recon Technical Report N

Wolfire, M. G., McKee, C. F., Hollenbach, D., & Tielens, A. G. G. M. 2003, *ApJ*, 587, 278

Ysard, N., Abergel, A., Ristorcelli, I., et al. 2013, *A&A*, 559, A133

Ysard, N., Juvela, M., & Verstraete, L. 2011, *A&A*, 535, A89

Ysard, N., Köhler, M., Jones, A., et al. 2016, *A&A*, 588, A44

Ysard, N., Köhler, M., Jones, A., et al. 2015, *A&A*, 577, A110

Ysard, N., Miville-Deschénes, M. A., & Verstraete, L. 2010, *A&A*, 509, L1

Ysard, N. & Verstraete, L. 2010, *A&A*, 509, A12

## Appendix A: Removal of zodiacal residual at 12 $\mu\text{m}$

The IRIS maps (Miville-Deschénes & Lagache 2005) were partially corrected for residual zodiacal emission, compared to the original IRAS products (ISSA plates – Wheelock et al. 1993). This was achieved by setting the emission at scales larger than 1° to the one of DIRBE that benefited from a better zodiacal subtraction (Kelsall et al. 1998). Nevertheless, the DIRBE and IRIS maps still show significant zodiacal residual, especially at 12 and 25  $\mu\text{m}$  (see Fig. A.1). Most of the zodiacal residual is oriented parallel to the ecliptic plane, but because of the scanning strategy of IRAS that was following the ecliptic plane, and of the way zero levels were estimated in the ISSA plates products, there are also residual perpendicular to the ecliptic plane.

In order to improve on the zodiacal residual subtraction in the IRIS 12  $\mu\text{m}$  band, we have performed an adaptative filtering tailored to extract residual emission oriented along or perpendicular to the ecliptic plane. The full methodology will be described in a forthcoming paper (Miville-Deschénes et al., in prep). Here we only summarise the steps of the processing.

The main difficulty to estimate the zodiacal residual from the map itself (and not going back to the original data timeline) is to separate it from the ISM emission itself that is dominating the signal almost everywhere. To estimate the zodiacal map,  $Z(\mathbf{r})$  of an emission map  $I(\mathbf{r})$  (here the IRIS 12  $\mu\text{m}$  map) we perform a filtering  $F$  of a residual map  $R(\mathbf{r})$ :

$$Z(\mathbf{r}) = F(R(\mathbf{r}))$$

where  $R$  is a difference map between the original map  $I$  and a reference map  $I_0$  (supposed free of zodiacal residual) times a spatially varying correlation coefficient  $\alpha$ :

$$R(\mathbf{r}) = I(\mathbf{r}) - \alpha(\mathbf{r})I_0(\mathbf{r}).$$

Here the reference map used is the 100  $\mu\text{m}$  map that combines the original IRIS map with the one of Schlegel et al. (1998) that has less zodiacal residual at large scales, also used in the all-sky dust model of Planck Collaboration et al. (2014a). It is available on the Planck archive.

The correlation coefficient  $\alpha(\mathbf{r})$  is estimated benefiting from the Healpix gridding of the data. Specifically,  $\alpha$  is estimated on a coarser Healpix grid (we used  $n_{\text{side}} = 32$ ) where, for each big Healpix pixel, the linear regression correlation coefficient is calculated using  $n_{\text{side}} = 2048$  pixels of  $I$  vs  $I_0$  encapsulated in the  $n_{\text{side}} = 32$  big pixels. This coarse map of  $\alpha$  is then regressed to  $n_{\text{side}} = 2048$  to calculate  $R(\mathbf{r})$ .

The filtering  $F$  applied on  $R$  is tailored to extract large-scale structures parallel and perpendicular to the ecliptic plane. To do so we filter  $R$  using a median filtering technique with an elongated window. First a window parallel to the ecliptic plane is used with a width of 20° in ecliptic longitude and only 3' in latitude (basically only two pixels). The map of  $Z$  found that way is removed from  $I$  and the whole process is reproduced using a perpendicular filtering window of 3' in longitude and 40° in latitude.

The resulting 12  $\mu\text{m}$  map obtained after this process is shown in Fig. A.1-right. Faint zodiacal residual are still visible but the improvement is significant. It can be evaluated by looking at correlation of the 12  $\mu\text{m}$  emission with other tracers of ISM column density. As example, in Fig. A.2 is presented the correlation of the original (top) and zodi-corrected (bottom) IRIS 12  $\mu\text{m}$  maps with  $\tau_{353 \text{ GHz}}$  (here converted to column density  $N_{\text{H}}$  Planck Collaboration et al. 2014a), convolved at a resolution of 1° and limited to pixels used in the current analysis (cf. mask shown in Fig. 1). The correlation coefficient is increased from 0.82 to 0.86.

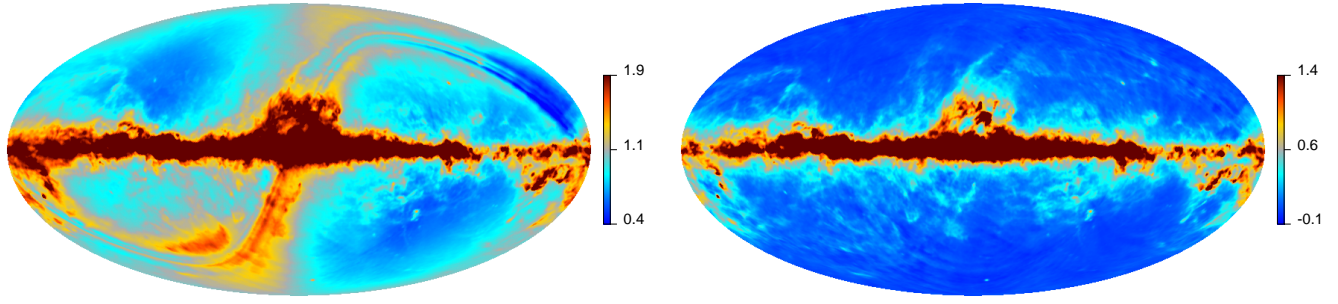


**Fig. A.1.** Left: All-sky IRAS 12  $\mu\text{m}$  map from the IRIS reprocessing (Miville-Deschénes & Lagache 2005). Right: IRAS 12  $\mu\text{m}$  map obtained after removal of the zodiacal residual.

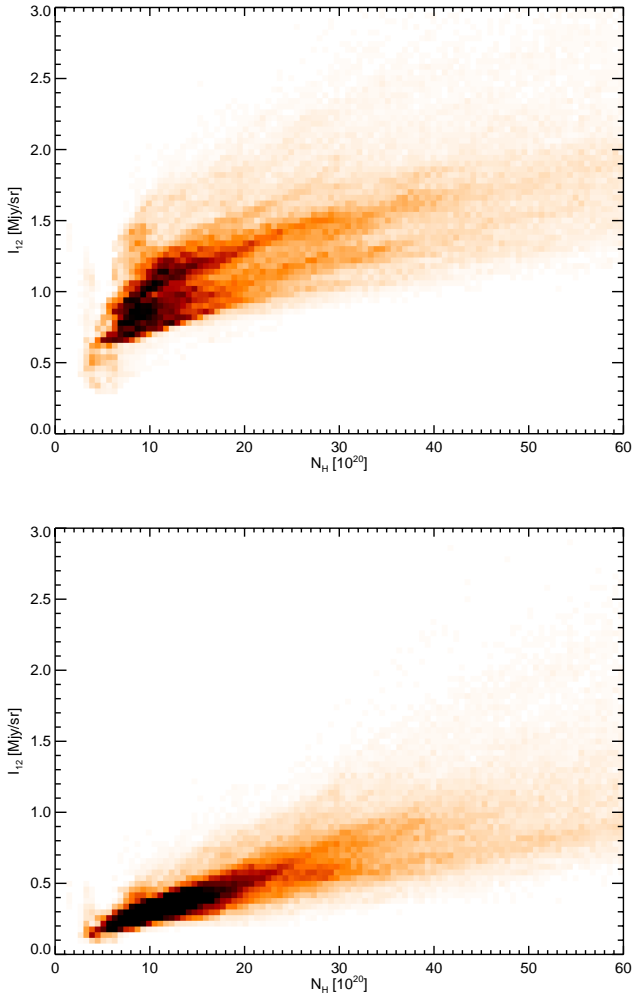


**Fig. A.2.** Two-dimensional histogram of the 12  $\mu\text{m}$  emission as a function of  $N_{\text{H}}$  deduced from the  $\tau_{353 \text{ GHz}}$  dust optical depth map of Planck Collaboration et al. (2014a), before (top) and after (bottom) zodiacal correction. The data are from the maps used in the current paper; all maps are at 1° resolution and only the pixels in the mask shown in Fig. 1 were used to build the histograms.